Photoacoustics 44 (2025) 100737

Contents lists available at ScienceDirect

Photoacoustics

journal homepage: www.elsevier.com/locate/pacs

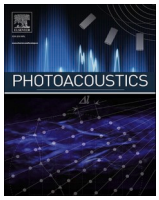

Photoacoustic imaging detects cerebrovascular pathological changes in sepsis

Zhigang Wang [a,1], Changpeng Ai [b,1], Ting Sun [c], Zhiyang Wang [a], Wuyu Zhang [a], Feifan Zhou [c,*], Shengnan Wu [b,*]

[a] MOE Key Laboratory of Laser Life Science & Institute of Laser Life Science, College of Biophotonics, School of Optoelectronic Science and Engineering, South China Normal University, Guangzhou 510631, China
[b] Key Laboratory of Brain Health Intelligent Evaluation and Intervention, Ministry of Education, School of Medical Technology, Beijing Institute of Technology, Beijing 100081, China
[c] Key Laboratory of Biomedical Engineering of Hainan Province, School of Biomedical Engineering, Hainan University, Sanya 572024, China

ARTICLE INFO

Keywords:
Photoacoustic microscopy
Sepsis-associated encephalopathy
Blood-brain barrier permeability
Cerebrovascular morphology
Cortical brain regions

ABSTRACT

Sepsis-associated encephalopathy (SAE) is a common complication of sepsis, involving acute brain dysfunction. Although cerebrovascular impairment plays a critical role in SAE, sepsis-induced microvascular changes remain poorly quantified. Here, we used photoacoustic microscopy to dynamically assess blood-brain barrier permeability in septic mice, analyzing vascular structure across five parameters. Additionally, we examined pathological changes in major cortical regions and conducted behavioral tests to validate the findings. Results showed microvascular degeneration, including reduced vascular density and branching, alongside an increase in fine vessels. Motor-related cortical areas were most affected, correlating with severe motor and cognitive deficits in septic mice. This study provides the first *in vivo*, multi-parametric analysis of sepsis-induced cerebrovascular pathology, revealing region-specific damage. Our findings directly link microvascular dysfunction to SAE progression and highlight photoacoustic microscopy's potential in neuroscience research.

1. Introduction

Sepsis is a systemic inflammatory response syndrome triggered by infection, often leading to multiple organ dysfunction, including brain injury[1]. Sepsis-associated encephalopathy (SAE), a common complication in septic patients, manifests as cognitive impairment, consciousness disturbances, and even coma, significantly affecting patient prognosis[2]. It affects up to 70 % of sepsis patients[3] and is associated with prolonged intensive care unit stays and increased mortality[4]. Although the pathological mechanisms of sepsis-induced brain injury remain incompletely understood, studies suggest that cerebrovascular dysfunction plays a critical role in its development. Given that mortality rises with SAE severity, early identification and management of SAE patients are crucial for reducing morbidity and mortality[5].

The pathophysiology of SAE is complex, involving multiple mechanisms, primarily characterized by systemic inflammation, blood-brain barrier (BBB) dysfunction, neuroinflammation, microcirculatory impairment, and their interactions with cerebral dysfunction. Microcirculatory dysfunction develops rapidly and precedes detectable changes in neurovascular coupling and systemic circulation. However, few clinically feasible methods exist for assessing cerebral microcirculation[6], and alterations in regional cerebral microcirculation in sepsis patients remain understudied. Fernando A. Bozza et al. employed magnetic resonance imaging to evaluate brain morphology and metabolism in a murine sepsis model[7], but the resolution limitations of magnetic resonance imaging restrict its utility for studying microvascular features. Yukio Imamura et al. utilized lead sulfide quantum dots for *in vivo* near-infrared fluorescence imaging of cerebral venous thrombosis in septic mice, confirming thrombus formation in cerebral vasculature[8]. However, second near-infrared imaging still lacks sufficient resolution and requires exogenous contrast agents for microvascular visualization.

In recent years, photoacoustic imaging (PAI) has emerged as a novel imaging modality that combines the high resolution of optical imaging with the deep penetration of acoustic waves, while offering non-invasive imaging potential. It utilizes hemoglobin in the blood as an endogenous

* Corresponding authors.
E-mail addresses: zhouff@hainanu.edu.cn (F. Zhou), wushengnan@bit.edu.cn (S. Wu).
[1] Both authors contributed equally to this work.

https://doi.org/10.1016/j.pacs.2025.100737
Received 6 April 2025; Received in revised form 19 May 2025; Accepted 27 May 2025
Available online 30 May 2025

contrast agent to achieve label-free imaging of living vasculature, enabling high-resolution visualization of vascular structures and hemodynamic changes. This characteristic makes PAI particularly valuable for studying vascular-related diseases[9]. Zhang et al. developed a small animal photoacoustic imaging system capable of providing a large field of view up to 20 mm × 20 mm, micrometer-level high resolution[10], offering new perspectives for investigating cerebrovascular pathological changes in sepsis.

This study pioneers the application of photoacoustic imaging technology for in-depth analysis and investigation of pathological alterations in the microvasculature of septic mice. Utilizing a 560 nm wavelength photoacoustic microscopy system, we achieved high-resolution imaging and quantitative characterization of pathological changes in murine microvessels. A murine sepsis model was established using cecal ligation and puncture (CLP) [11,12]. Using Evans Blue (EB), we observed the disruption of BBB in septic mice through continuous monitoring and systematically characterized the pathological features of microvasculature from multiple morphological perspectives. Furthermore, we conducted an analysis of vascular pathological changes in major cortical brain regions and correlated these findings with behavioral phenotypes. By employing *in vivo* imaging approaches, this study establishes a clearer link between sepsis-induced microvascular pathology and impairments in motor and cognitive memory functions.

2. Materials and methods

2.1. Animals preparation

Male C57BL/6 J wild-type mice (6–12 weeks) from SPF Biotech (Beijing, CN) were maintained in individually ventilated cage systems with controlled photoperiod (12 h light/dark cycle). All animal experiments were approved by Hainan University IACUC. No animals were reused across different experiments and all experimental groups were independent.

2.2. Animal experimental model

Isoflurane-anesthetized mice underwent midline laparotomy (1 cm) following abdominal preparation. The cecum was exteriorized, ligated with 5–0 silk suture, and punctured with a 21 G needle at the distal terminus. Minimal fecal extrusion was achieved through gentle compression prior to organ repositioning. Sham controls received equivalent surgical manipulation omitting cecal ligation/puncture. All subjects underwent layered abdominal closure with postoperative fluid resuscitation (5 mL/100 g normal saline, intraperitoneal).

2.3. Tail vein injection of EB

EB (Sigma-Aldrich, US) was dissolved in ultrapure water to prepare a 2 % EB solution. Before injection, the solution was pre-warmed to 37°C to reduce irritation to the mice. A mouse restrainer (such as a transparent plastic restraint tube) was used to immobilize the mice and expose the tail. The tail was wiped with 75 % ethanol to disinfect and dilate the tail vein. A syringe (1 mL) was used to aspirate 200 μL of the 2 % EB solution. The needle was inserted slowly into the vein at an angle of approximately 30° at a relatively thick portion of the tail vein. After confirming the needle had entered the vein, the solution was slowly injected (injection time approximately 10–15 s). After completion of the injection, a sterile cotton ball was used to apply gentle pressure to the injection site to stop bleeding. The mice were observed post-injection to ensure no abnormal reactions (such as dyspnea, convulsions, etc.).

2.4. Laser speckle imaging

The laser speckle imaging system (Wuhan Xunwei Optoelectronic Technology Co., Ltd, CN) utilized an excitation laser wavelength of 785 nm. Mice were maintained under anesthesia using isoflurane gas. Hair removal was performed on the mouse brain area using clippers and depilatory cream, followed by scalp removal with surgical scissors. A brain fixation device (PA-BR101, Guangdong Optoacoustic Technology Co., Ltd, CN) was employed to maintain stability during imaging. Laser speckle imaging signals were acquired by a charge coupled device camera and transmitted to a computer, with image reconstruction and data visualization performed using SIM BFI software. The cortical region of experimental mice was selected for data analysis.

2.5. Photoacoustic imaging

Imaging was conducted using a small animal photoacoustic imaging system (PASONOANI, Guangdong Photoacoustic Technology Co., Ltd., CN). A 560 nm Raman all-solid-state pulsed laser (SHSL-50–560, Nanjing Institute of Advanced Laser Technology; pulse width: ≤ 8 ns) was triggered at a repetition rate of 10 kHz. The laser beam was transmitted via an optical fiber coupler (PAF2–7A, Thorlabs) and collimated using a fiber collimator (F240FC, Thorlabs). The collimated beam was then reflected by a 45° dichroic mirror (GCC-414008, Daheng Optics, CN) and focused through a 4 × objective lens (GCO-2111, Daheng Optics, CN) onto the sample. Photoacoustic signals were generated using a custom-designed ultrasonic transducer (piezoelectric material, polyvinylidene fluoride; center frequency, 30 MHz; bandwidth, 80 %, −6 dB; outer diameter, 8 mm; central aperture diameter, 3 mm; focal length, 8 mm).

The signals were amplified by a 50 dB gain amplifier (LNA-650, RF Bay, US) and digitized using a high-speed data acquisition card (200 Ms/s, m4i.4480 ×8, Spectrum, CER). System synchronization—including laser triggering, motorized stage movement, and PA signal acquisition—was controlled via an FPGA. Image acquisition and reconstruction were performed in real-time using PAM 2.0 software (Guangdong Photoacoustic Technology Co., Ltd.), developed in C+ + and Qt[10].

First, mice were anesthetized, and hair was removed from mice using razors and depilatory cream, followed by scalp removal while preserving skull integrity. During scanning, a brain fixation device (PA-BR101, Guangdong Optoacoustic Technology Co., Ltd, CN) was used to secure the mouse brain, significantly ensuring positional stability during the experiment. By adjusting the relative positions of the 4 × objective lens and ultrasound transducer, the 560 nm laser and ultrasound focal points were aligned to achieve optimal photoacoustic detection efficiency. The motorized translation stage moved the mouse in the x and y directions for raster scanning. During scanning, an appropriate amount of water was required as coupling medium both in the water tank and on the surface of the biological sample, with the transducer front end immersed in water. The scanning range of 10 mm × 10 mm × 2.4 mm was sufficient to cover the mouse brain, with a fast-axis scanning speed of 10 mm/s and total scanning time of approximately 8 minutes. Laser energy was maintained within safe limits to prevent thermal damage while ensuring high signal-to-noise ratio imaging.

2.6. Quantitative analysis of vascular morphological parameters

Vascular density, porosity, and branching index were calculated directly or indirectly using the vascular analysis software AngioTool [13].

Vascular density (VD) refers to the total length of blood vessels per unit area. It is defined as the ratio of the pixel area occupied by blood vessels to the total area of the analyzed region, reflecting the spatial distribution density of blood vessels within a given area.

$$VD = \frac{Total\ vessel\ area}{Total\ area} \tag{1}$$

Branching index (BI) represents the number of vascular bifurcation points per unit area, calculated as the ratio of total vascular branch points to the total analyzed area, which characterizes the complexity of the vascular network branching.

$$\mathrm{BI} = \frac{\textit{Total number of junctions}}{\textit{Total area}} \tag{2}$$

In this study, Lacunarity refers to Mean E Lacunarity, which is used to evaluate the sparsity of vascular networks. A higher value indicates uneven distribution of blank areas, suggesting the possible presence of either larger blank areas or clustered blank regions. First, AngioTool segments the image into vascular regions and blank regions. Sliding windows of different sizes are used to scan the image. For each window, its Lacunarity is defined as the variance and mean of pixel intensity in the blank region. The average of Lacunarity across all window sizes yields the Mean E Lacunarity.

$$\mathrm{Lacunarity} = \frac{\textit{Variance of pixel intensity}}{\textit{Mean pixel intensity}^2} \tag{3}$$

Vascular tortuosity and diameter statistics were performed in MATLAB (version R2023b; MathWorks, Natick, MA, US). First, median filtering was applied to the raw data to remove noise signals and improve the signal-to-noise ratio, followed by threshold segmentation and image binarization. The vascular skeleton was extracted, and branch points and endpoints in the skeleton were detected. The skeleton was disconnected in small regions near branch points, with each segment marked as an independent vessel. Using the vascular centerline as a search guide, Euclidean transformation was performed on the binarized image, and the average distance between the two edges of the vessel was calculated as the vessel diameter. Vascular tortuosity was quantified by the ratio of the actual length of each vessel to its Euclidean length (tortuosity index = actual length/Euclidean length), where a higher value indicates greater vascular tortuosity[14].

2.7. Method for analyzing BBB permeability

Processing and analysis of photoacoustic (PA) images were performed using ImageJ. The Percentile thresholding method was employed to eliminate pixels with lower intensities, thereby enhancing the visualization of EB leakage. For each time point before and after EB injection, PA (photoacoustic) images were segmented using a consistent fixed threshold, followed by pixel counting. An unpaired t-test was performed to compare the pixel counts between the 5-min and 60-min groups at their respective time points. The mean leakage at each time point was calculated by subtracting the pre-injection baseline pixel count from the averaged post-injection pixel count. Time-dependent leakage profiles for each group were subsequently fitted using Origin software.

2.8. Behavioral experiments

Open field test (OFT) was performed on postoperative day 5 to assess locomotor activity and anxiety-like behavior[15]. Subjects freely explored a white cubic box (40 × 40 × 40 cm) for 10 minutes. Movement parameters (speed, distance and time in center) were quantified using Visutrack (Xinruan Tech, CN).

The new object recognition (NOR) test has three phases: (1) Training (10 minutes of free exploration of two identical objects); (2) Interval (interval 1 hour, replace an old object with a new object); (3) Test (10 minutes of free exploration). Cognitive performance is calculated as follows:

$$\text{Recognition index}(\%) = \frac{\textit{Tnovel}}{\textit{Tnovel} + \textit{Tfamiliar}} \text{x}100\% \tag{4}$$

$$\text{Differentiation index} = \frac{\textit{Tnovel} - \textit{Tfamiliar}}{\textit{Tnovel} + \textit{Tfamiliar}} \tag{5}$$

Where T_{novel} and $T_{familiar}$ represent object exploration time.[16]

2.9. Anesthesia and brain extraction

Mice were anesthetized with isoflurane until reaching a state of deep coma, followed by euthanasia via cervical dislocation. The mice were secured on a dissection board, and their scalps were incised with scissors to expose the skull. Using bone scissors, the skull was carefully opened along the midline, and the cranial bones were gently removed to fully expose the brain. A curved forceps was used to delicately separate the brain tissue from the skull base, allowing for complete brain extraction.

2.10. Enzyme-linked immunosorbent assay (ELISA)

The whole blood of mice was collected by orbital blood collection 6 hours post-surgery. The serum was separated by centrifugation at 3000 rpm for 10 minutes. The serum samples were stored at −80℃ for future use. The commercial ELISA kits (purchased from NeoBioscience Technology Co., Ltd. CN) were used for operation in accordance with the instructions to detect the concentrations of interleukin 6 (IL-6) and tumor necrosis factor alpha (TNF-α) in the serum. The absorbance values were measured using an enzyme-linked immunosorbent assay reader at a wavelength of 450 nm, and the concentrations of the target factors in the samples were calculated based on the standard curve.

2.11. Organ function evaluation

The indicators such as direct bilirubin, total bilirubin, alanine aminotransferase, aspartate aminotransferase, blood urea nitrogen and creatinine in serum were determined by the automatic biochemical analyzer. The operation process was strictly carried out in accordance with the equipment operation procedures and the instructions of the reagent kit.

2.12. Data analysis

PA image processing was performed in ImageJ software (Fiji, version 2.14.0 National Institutes of Health, US). Statistical analysis was conducted using independent samples T-test ($^{*}P < 0.05$, $^{**}P < 0.01$, $^{***}P < 0.001$, $^{****}P < 0.0001$), with graphical representations created using GraphPad Prism software (version 10.2.2; GraphPad Software, San Diego, CA, US). All data are presented as mean ± standard error of the mean.

3. Results and analysis

3.1. Photoacoustic imaging system and material characterization

The photoacoustic microscopy (PAM) system employed in this study is illustrated in Fig. 1(a). To characterize the spatial resolution, we imaged the sharp edge of a surgical blade. As shown in Fig. 1(b-c), the edge spread function was used to fit the data at the edge of the maximum amplitude projection image. The lateral resolution of the PAM system was calculated to be 12.1 μm from the line spread function. The axial resolution was measured to be 69.3 μm through Hilbert transform analysis of the A-line signals.

Small amounts of blood and EB samples were drawn into capillaries, photographed in the same field of view, and subjected to PA imaging in Fig. 1(d). As shown in Fig. 1(e). Quantitative analysis of their PA amplitudes showed nearly identical photoacoustic signal intensities[17,18].To characterize the absorption properties of blood and EB at 560 nm, we diluted the samples at the same ratio and measured their absorption spectra between 400 nm - 700 nm using a microplate reader. Both blood and EB showed strong absorption at 560 nm (Fig. 1(f-g)).

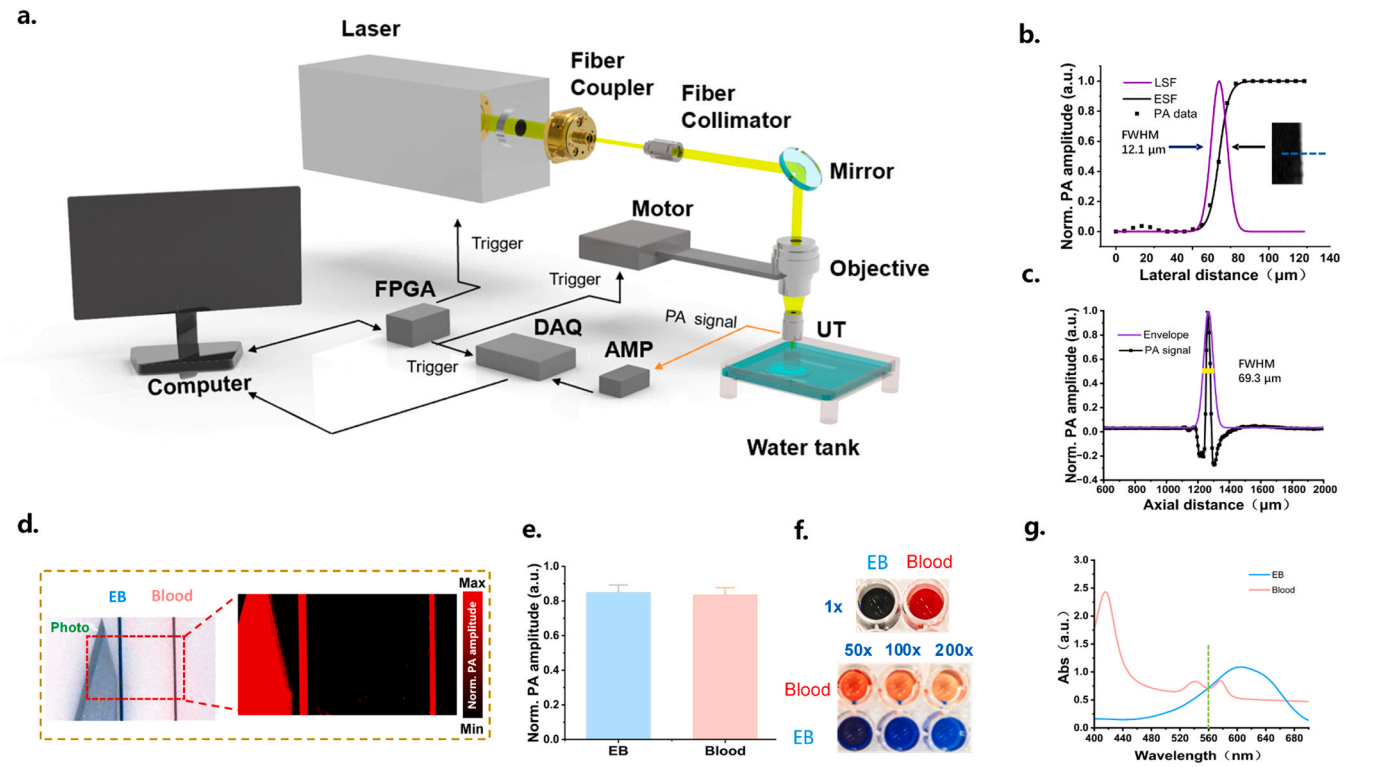

Fig. 1. Schematic of the photoacoustic imaging system and material characterization. (a) Diagram of the 560 nm photoacoustic microscopy (PAM) system. (b) Lateral resolution of the PAM system. (c) Axial resolution of the PAM system. (d) Photographs and corresponding PAM images of blood and Evans Blue (EB) samples. (e) Comparison of PA amplitudes between blood and EB. (f) Photographs of blood and EB samples. (g) Absorption spectra of blood and EB from 400 to 700 nm, showing strong absorption at 560 nm. Data plotting and curve fitting were performed using Origin software. Abbreviations: AMP, amplifier; FWHM, full width at half maximum; DAQ, data acquisition system; FPGA, field-programmable gate array; UT, ultrasonic transducer; LSF, the line spread function; ESF, the edge spread function; abs, absorbance; a.u., arbitrary unit.

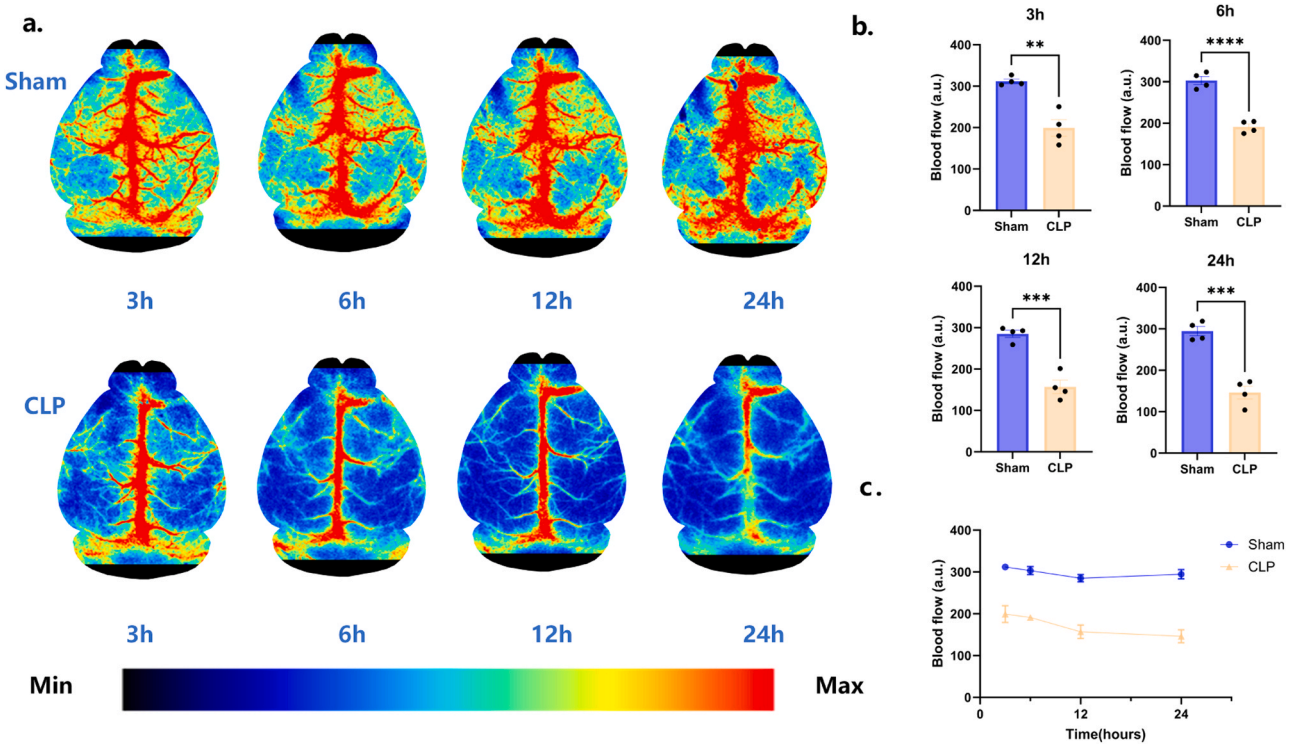

Fig. 2. Results of laser speckle blood flow imaging within 24 hours after cecal ligation and puncture (CLP) ($n = 4$). (a.) Laser speckle blood flow images of CLP group and Sham group within 24 hours. (b.) *T*-test results of laser speckle blood flow imaging between CLP mice and Sham mice at four time points (3 hours, 6 hours, 12 hours, 24 hours), with the most significant difference observed at 6 hours. (c.) Trend analysis of laser speckle blood flow imaging within 24 hours after CLP.

3.2. Investigation of cerebral blood flow changes in septic mice using laser speckle imaging

Sepsis-associated encephalopathy is an acute brain injury, with altered cerebral blood perfusion being one of its primary pathological characteristics[19]. Accordingly, we performed laser speckle blood flow imaging on both the CLP group and Sham group at 3 hours, 6 hours, 12 hours, and 24 hours post-modeling, followed by *t*-test analysis of the results. The time point showing the most significant differences in the *t*-test results was selected for photoacoustic imaging monitoring. Fig. 2 presents the results of the laser speckle blood flow imaging.

The experimental results showed that cerebral blood flow in CLP mice was significantly reduced compared to Sham mice, with the most pronounced difference observed at 6 hours post-CLP. Based on these findings, we inferred that cerebrovascular damage in septic mice might be most severe at 6 hours after CLP. Therefore, subsequent investigations of blood-brain barrier permeability were conducted at the 6-hour time point after CLP.

3.3. Evaluation of Systemic Inflammation Levels and Organ Function in Sepsis Mice

Since SAE is typically accompanied by systemic inflammatory response and multiple organ dysfunction, therefore, serum was harvested from mice 6 hours after CLP surgery to measure inflammatory cytokine levels and assess liver and kidney function, using ELISA and biochemical assays. The results showed that pro-inflammatory cytokines IL-6 and TNF-α were significantly elevated in the CLP group, indicating a systemic inflammatory response. Additionally, liver damage markers—bilirubin, alanine aminotransferase, and aspartate aminotransferase—as well as kidney damage markers—blood urea nitrogen and creatinine—were also significantly increased.

These findings demonstrate that the CLP-induced sepsis model exhibits significant inflammatory responses and liver/kidney dysfunction as early as 6 hours post-surgery, suggesting its suitability for studying the early stages of SAE.

3.4. Photoacoustic imaging reveals increased cerebrovascular permeability in septic mice

The blood-brain barrier consists mainly of microvascular endothelial cells interconnected by tight junction proteins, along with astrocytic end-feet, pericytes, and the basement membrane of capillaries. During sepsis, impairment of the BBB disrupts the central nervous system's protective isolation. This breach permits neurotoxic compounds to infiltrate the central nervous system, inducing direct neuronal injury and worsening glial cell activation. Consequently, a cascade of neuroinflammatory responses is initiated[20–23]. During the progression of sepsis, the disruption of BBB and structural integrity constitutes a central pathological link in the development of central nervous system dysfunction and subsequent multi-organ damage[6]. Although the mechanisms underlying sepsis-induced BBB injury are not fully understood, increased BBB permeability during sepsis is increasingly recognized.

As shown in Fig. 3(a), we utilized the strong specific absorption of EB at 560 nm wavelength to perform continuous whole-brain PA imaging on both CLP and Sham groups at 6 hours post-surgery. Imaging was conducted at multiple time points: before EB injection, and at 5 minutes, 15 minutes, 30 minutes, 45 minutes, and 60 minutes after tail vein injection. This approach enabled quantitative assessment of EB extravasation for dynamic evaluation of BBB permeability[24].

Fig. 3(b-c) displays photoacoustic images of the CLP and Sham groups within 60 minutes. To better highlight EB leakage, the original PA images were subjected to threshold segmentation and region of interest display. Visually, CLP mice exhibited extensive EB leakage in the frontal and parietal lobes, while Sham mice showed EB leakage mainly concentrated near the coronal, sagittal, and lambdoid sutures. Studies have indicated that the meningeal vascular system, including vasculature at cranial sutures, closely interacts with BBB, regulating immune cell trafficking and inflammatory responses[25]. The meningeal vessels

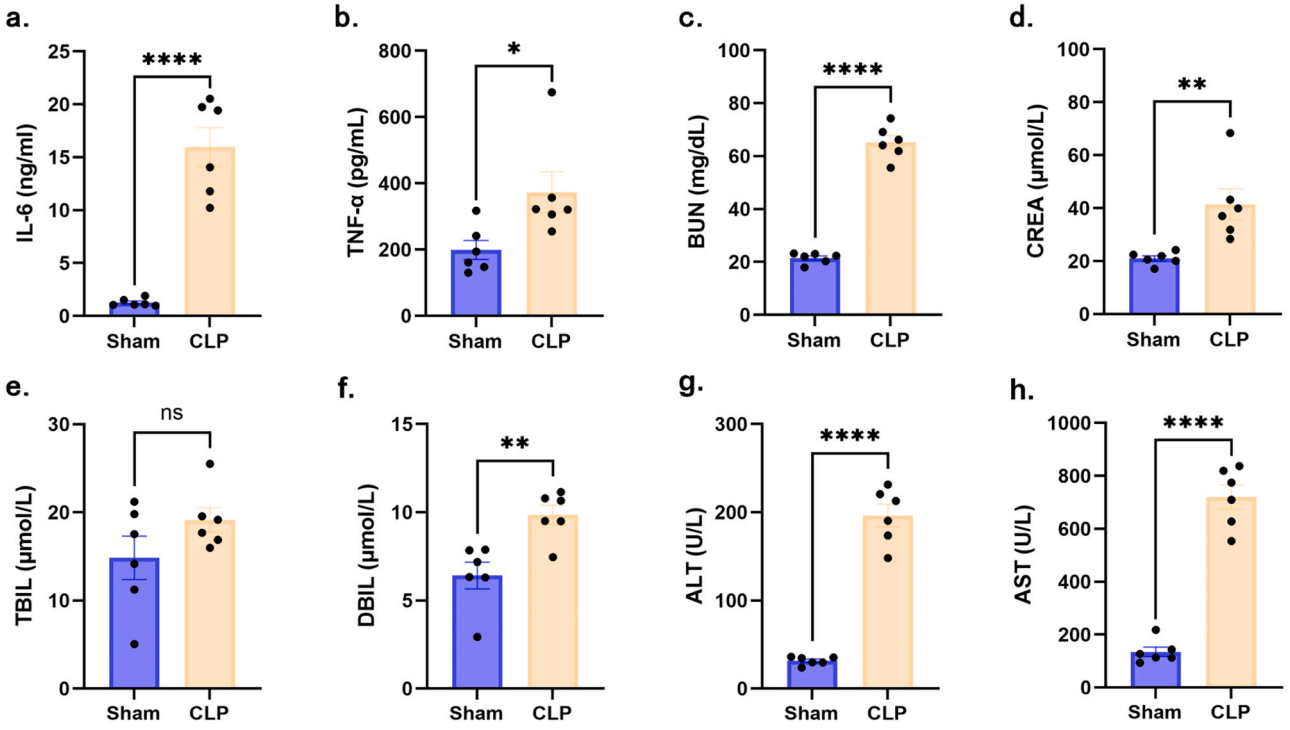

Fig. 3. Evaluation of inflammatory cytokine levels and liver/kidney function 6 hours after CLP modeling ($n = 6$). (a.) Interleukin 6 (IL-6). (b.) Tumor necrosis factor alpha (TNF-α). (c.) Blood urea nitrogen (BUN). (d.) Creatinine (CREA). (e.) Total bilirubin (TBIL). (f.) Bilirubin (DBIL). (g.) Alanine aminotransferase (ALT). (h.) Aspartate aminotransferase (AST).

near cranial sutures exhibit higher vascular density and unique hemodynamic properties[26,27], which may contribute to increased permeability.

As shown in Fig. 4(d), the trends in average PA intensity and EB leakage area over 60 minutes were similar between CLP and Sham mice, but the changes were more pronounced in CLP mice. The time-derivative fitting curve of EB diffusion reflected the leakage rate, with the CLP group demonstrating a higher overall diffusion speed than the Sham group within 60 minutes. CLP mice began to show diffuse leakage as early as 5 minutes. The mean EB leakage in the CLP group was 72.5 % greater than that in the Sham group at 5 minutes in Fig. 4(f). After 60 minutes, the average PA intensity and leakage area in the CLP group were 53.4 % and 56.7 % higher, respectively, than those in the Sham group, shown in Fig. 4(e). As illustrated in Fig. 4(h), excised whole brains of mice (without perfusion) were photographed 60 minutes after EB injection, clearly showing increased EB content in the brain parenchyma of CLP mice compared to Sham mice. The EB diffusion regions in the cerebral cortex aligned with the PA image analysis results. Fig. 4(i) shows representative continuous PA imaging after vehicle solution injection at 6 hours post-CLP, where no leakage signal was observed, ruling out potential interference from the vehicle solution. The statistical results of average PA intensity at 60 minutes are presented in Fig. 4 (g), showing almost no difference between the two groups. These experimental findings further demonstrate the potential of *in vivo* PA imaging in exploring, preventing, and treating BBB-related injuries.

3.5. Morphological transformations of cerebral vasculature in sepsis

Accumulating evidence supports that alterations in cerebral microcirculation during sepsis may play a significant role in SAE pathogenesis. These changes, together with BBB dysfunction, modify the brain's extracellular environment, impair cerebral function, and may contribute to SAE development and progression[6]. Studies have demonstrated that sepsis releases pro-inflammatory factors that disrupt central nervous system homeostasis and damage cerebral microcirculation, including impairment of cerebrovascular vasomotor regulation and blood pressure autoregulation[28]. This leads to progressive microvascular occlusion extending beyond initial obstruction sites, thereby exacerbating focal ischemia, compromising cerebral perfusion, and aggravating brain injury[19].

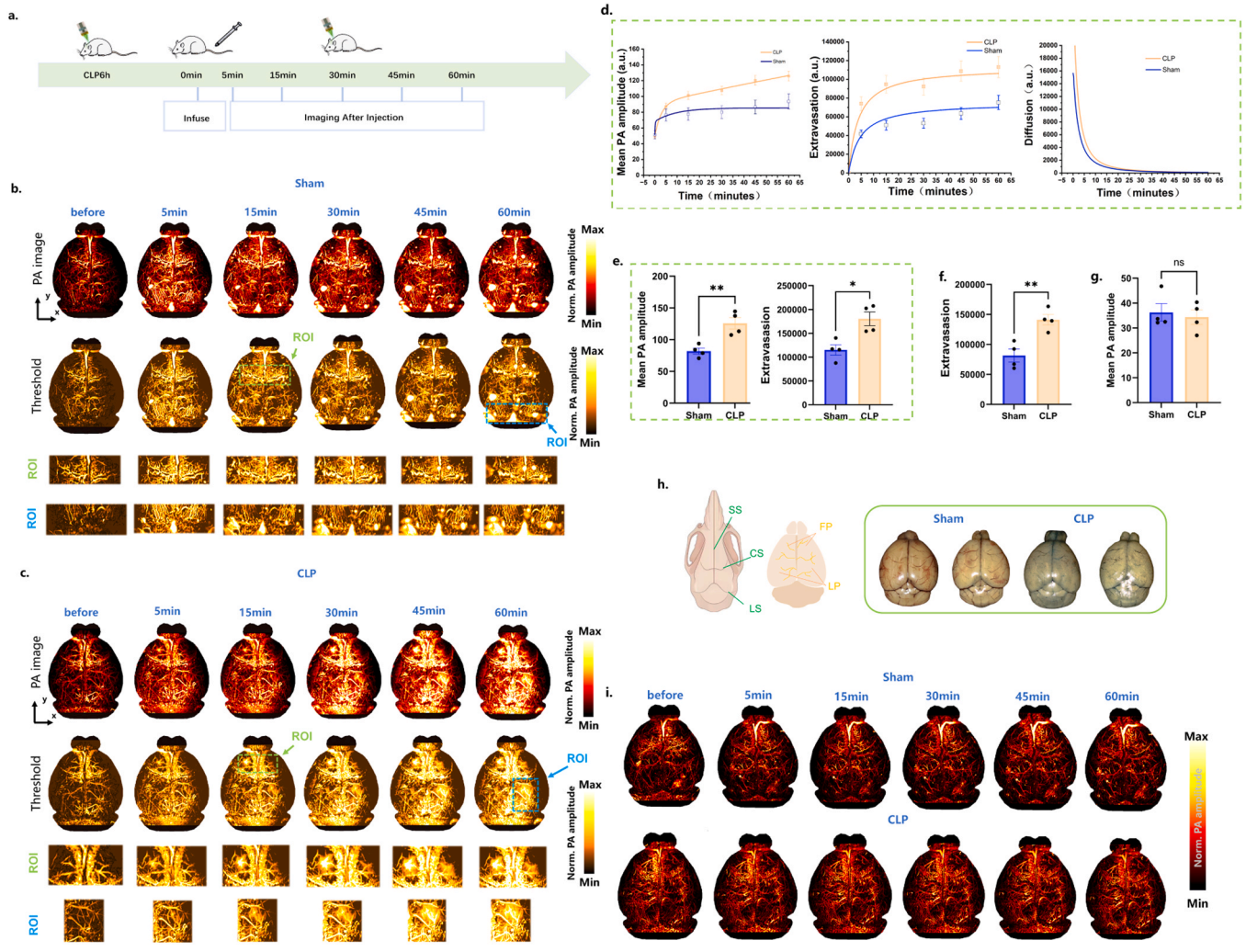

Fig. 4. Continuous photoacoustic *in vivo* imaging monitoring and analysis within 60 minutes after EB injection at 6 hours post-CLP modeling ($n = 4$). (a.) Experimental procedures including modeling, EB carrier solution injection, and photoacoustic (PA) imaging. (b.) Sequential PAM images of Sham group post-EB injection. (c.) Sequential PA imaging of CLP group post-EB injection. (d.) Trend of average PA amplitude changes in CLP and Sham groups post-EB injection, EB leakage trends in CLP and Sham groups and EB leakage rates in CLP and Sham groups. (e.) Static comparison of average PA intensity and EB leakage between CLP and Sham groups at 60 minutes. (f.) EB leakage comparison between CLP and Sham groups at 5 minutes. (g.) mean PA intensity comparison between CLP and Sham groups at 60 minutes post-vehicle solution injection. (h.) Photographs of mouse brains at 60 minutes post-EB injection. (i.) Continuous PA imaging after vehicle solution injection at 6 hours post-CLP.

To investigate sepsis-induced microvascular morphological changes, we performed PA imaging on CLP mice at 24 hours and 7 days post-surgery and conducted quantitative analysis of PA images from five aspects: vascular density, branching index, porosity, tortuosity, and statistics of vessels with different diameters[13,14].

Fig. 5(a-b) shows the fused neurovascular images of whole-brain meninges and cerebral cortex, displaying clear and complete vascular networks. As shown in Fig. 5(c), at 24 hours post-modeling, there were minimal differences in all parameters between CLP and Sham mice.

Since inflammation is often accompanied by a series of pathological vascular changes, Fig. 5(d) demonstrates that at 7 days post-modeling, compared to Sham mice, CLP mice showed significantly reduced branching index and vascular density. A slight increase in porosity and tortuosity was observed, suggesting that the microvasculature in septic mice may have become sparser and more tortuous. The diameter distribution analysis revealed an increased proportion of vessels < 60 μm and decreased proportion of vessels > 60 μm in CLP mice at 7 days, as indicated in the figure.

These changes may be related to inflammatory mediators (such as cytokines and reactive oxygen species) inducing cerebral microvascular constriction and reduced blood flow. Inflammatory mediators including TNF-α and IL-1β disrupt angiogenesis and promote vascular degeneration, leading to significantly reduced vascular density and branching index, impairing the brain's ability to maintain adequate blood supply, and further exacerbating cognitive decline[29–31].

3.6. *Vascular pathological changes in different brain regions of septic mice*

Research evidence indicates that sepsis differentially impacts distinct brain regions, with the cerebral cortex and hippocampus exhibiting particularly high vulnerability[32]. However, there are currently almost no studies on microvascular pathological changes caused by sepsis-associated encephalopathy in different brain regions.

In this study, we used PA imaging to conduct in-depth analysis of major cortical regions in mice from two aspects: BBB permeability and microvascular morphology. Primary motor cortex (M1) is responsible for planning and initiating voluntary movements[33]; Secondary motor cortex (M2) is involved in movement planning, coordination and execution of complex movements[34]; Retrosplenial dysgranular cortex (RSD) is closely related to spatial navigation, memory integration and episodic memory[35]; Primary visual cortex (V1) and secondary visual cortex (V2) are cortices involved in visual information acquisition and processing[36,37]. Referencing the Allen Brain Atlas[38], we initially registered the PA images in ImageJ, followed by fine adjustments and segmentation of individual brain regions in Photoshop.

As shown in Fig. 6(b), septic mice showed significantly increased EB leakage in all brain regions compared to Sham mice, with the motor-related regions M1/M2 being the most prominent. The average PA intensity results in each brain region showed the same pattern as the leakage results (Fig. 6(c)). These results indicate that the BBB was disrupted in all three brain regions, with the most severe damage occurring in the M1/M2 regions.

Corresponding to these findings, as shown in Fig. 6(d-f), the vascular morphology analysis also showed the most significant changes in the M1/M2 regions, where vascular density and branching index significantly decreased, porosity increased, and tortuosity significantly increased. This suggests that microvascular degeneration was most severe in these regions, with markedly reduced vascular area, impaired uniformity of vascular networks, and characteristics of significantly sparser and more tortuous vascular distribution. Fig. 7

The RSD region showed similar trends to the M1/M2 regions, with significantly increased tortuosity but no obvious changes in other parameters. In the V1/V2 regions, vascular density decreased but not significantly, branching index slightly increased (which may reflect individual variation based on data distribution), and both porosity and

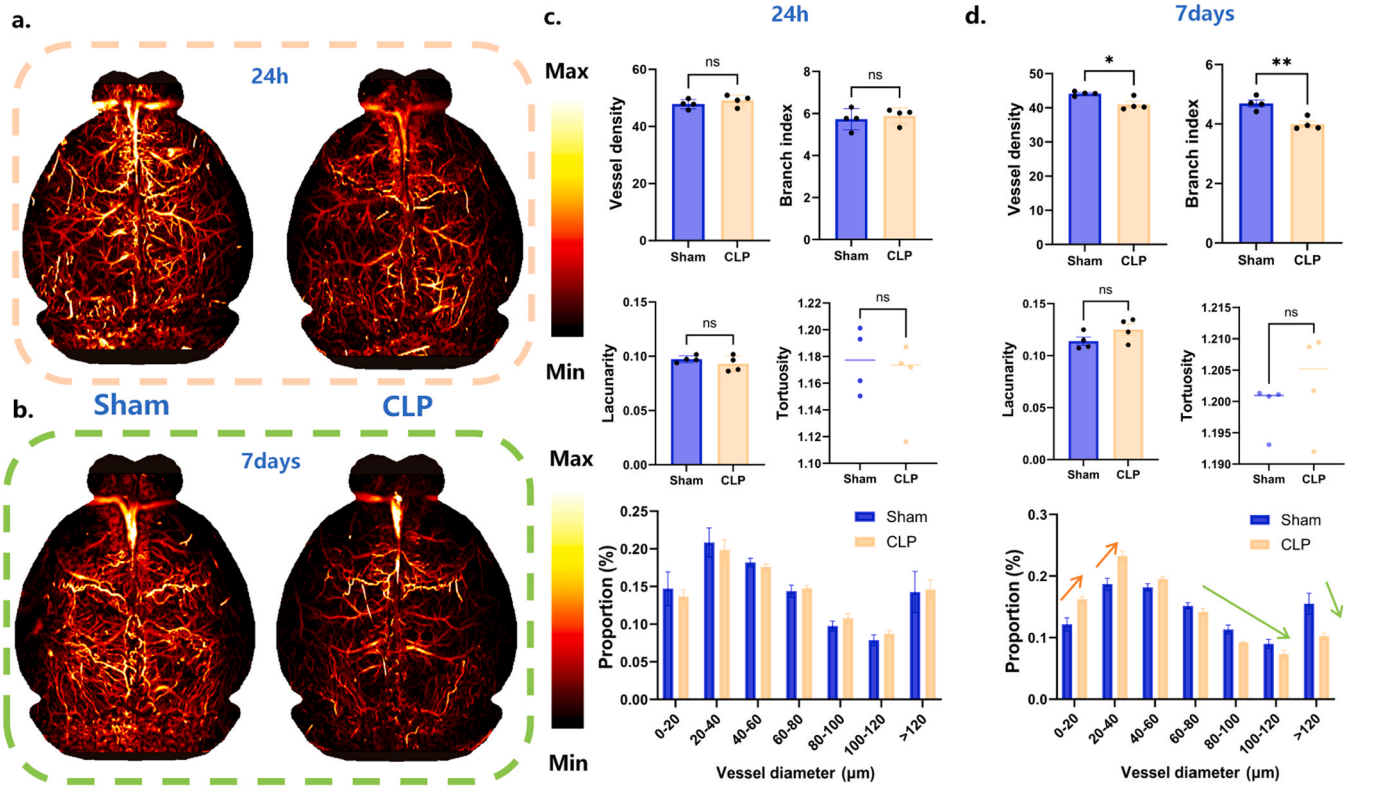

Fig. 5. PA imaging and analysis of vascular morphology in CLP mice at 24 hours and 7 days post-CLP ($n = 4$). (a.) Representative PA images of cerebral cortex in CLP and sham mice at 24 hours post-CLP. (b.) Representative PA images of cerebral cortex in CLP and sham mice at 7 days post-CLP. (c.) Quantitative analysis of vascular morphology in CLP and sham mice at 24 hours post-CLP. (d.) Quantitative analysis of vascular morphology in CLP and sham mice at 7 days post-CLP.

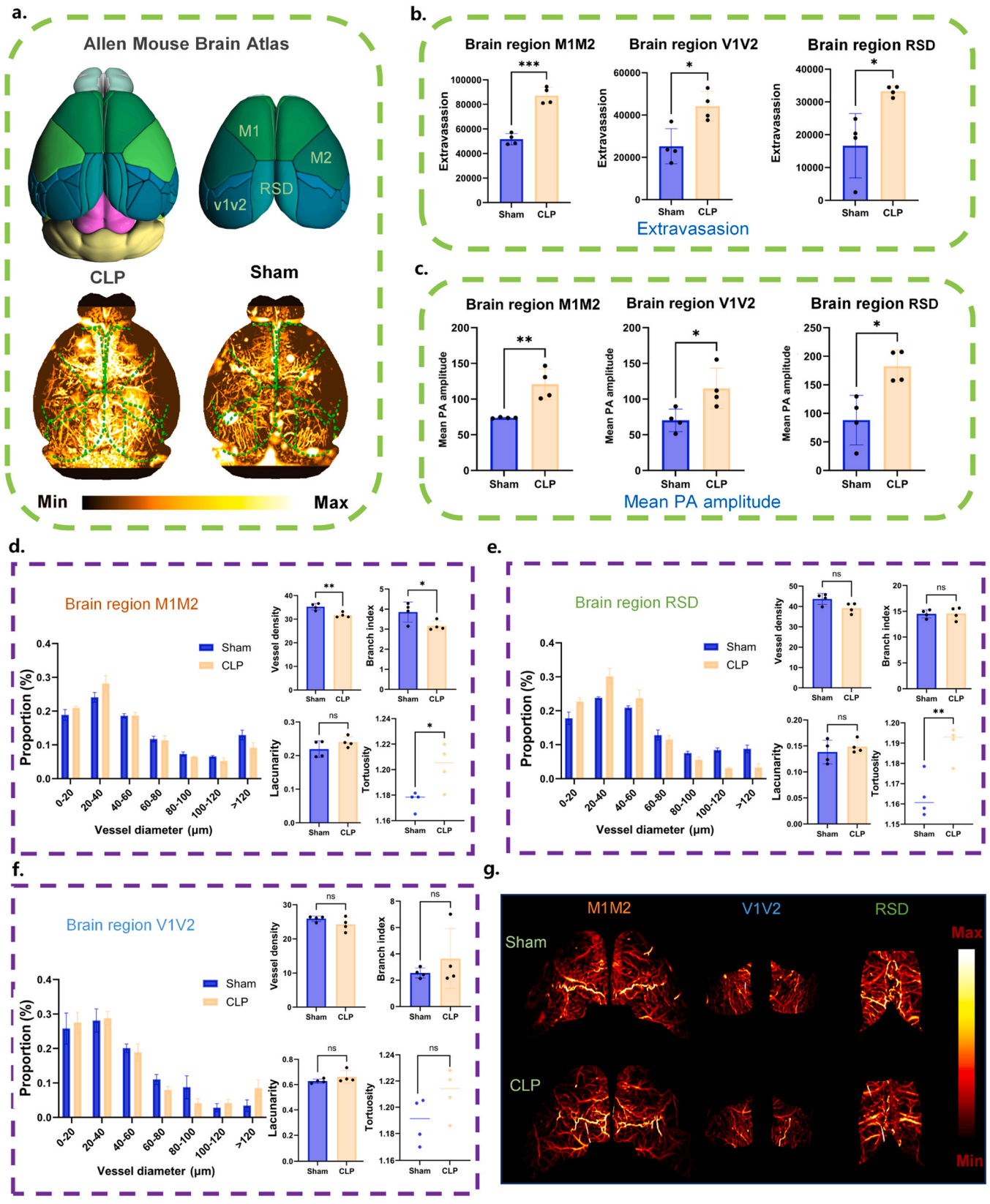

Fig. 6. Quantitative analysis of blood-brain barrier (BBB) permeability and pathological changes in microvascular morphology across different brain regions. (a.) Schematic division of the Allen Brain Atlas and major brain regions on representative PA images demonstrating EB diffusion. (b.) Quantitative analysis of EB diffusion in different brain regions 6 hours post-CLP. (c.) Quantitative analysis of mean PA intensity in different brain regions 6 hours post-CLP. (d.) Quantitative analysis of vascular morphological changes in primary motor cortex (M1)/secondary motor cortex (M2) brain regions 7 days post-CLP. (e.) Quantitative analysis of vascular morphology in primary visual cortex (V1)/secondary visual cortex (V2) brain regions 7 days post-CLP. (f.) Quantitative analysis of vascular morphology in retrosplenial dysgranular cortex (RSD) brain regions 7 days post-CLP. (g.) Representative PA images showing segmented microvasculature in different brain regions at 7 days post-CLP.

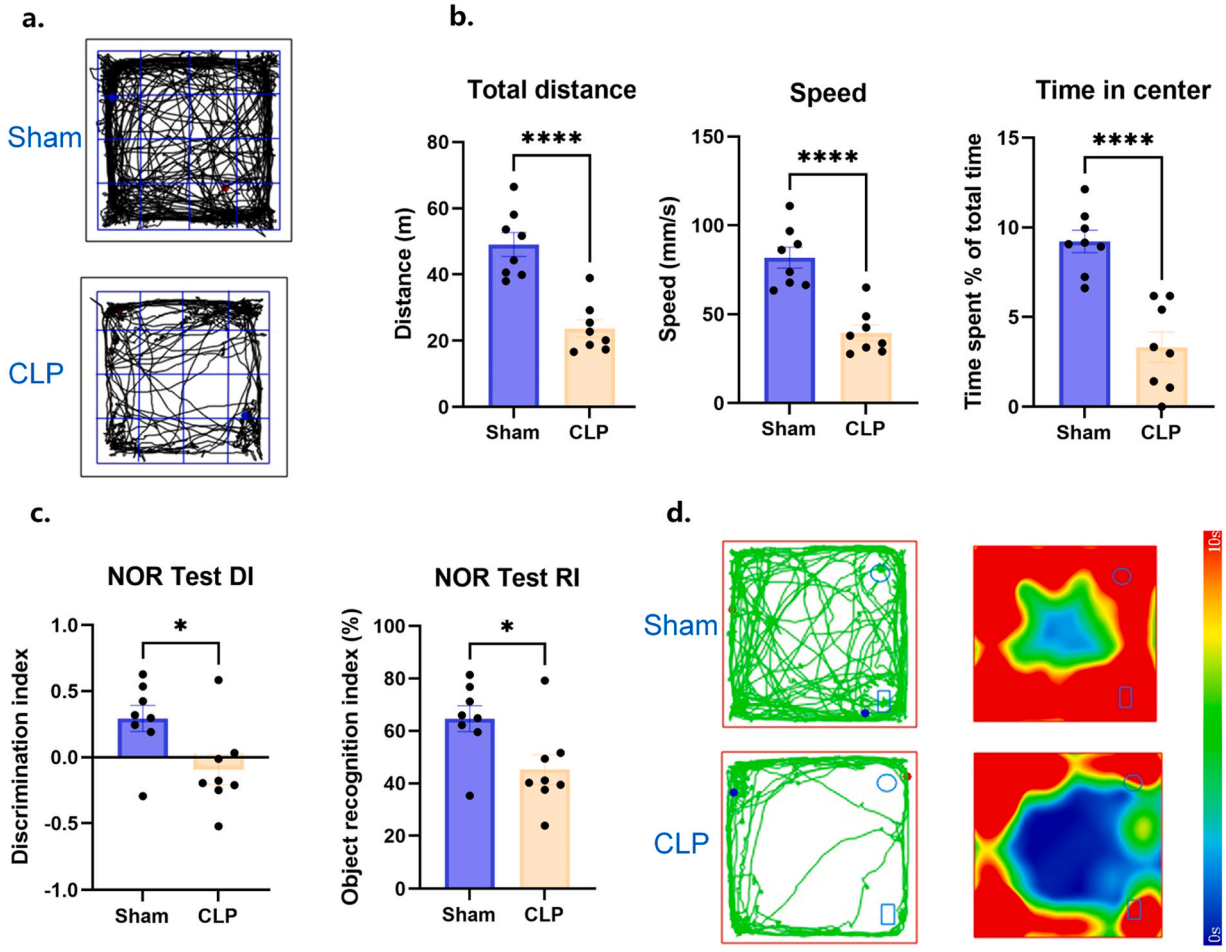

Fig. 7. Motor and cognitive memory performance of Sham and CLP mice ($n = 8$). (a.) Movement trajectories of Sham and CLP mice in open field test. (b.) Comparison of three behavioral parameters in open field test: total distance, speed, and percentage of time spent in center area (Time in center % of total time). (c.) Comparison of two cognitive parameters in new object recognition (NOR): discrimination index (DI) and recognition index (RI). (d.) Exploration heatmaps of Sham and CLP groups in NOR test.

tortuosity increased.

Overall, all three brain regions showed an increased proportion of vessels < 40 μm and a decreased proportion of vessels > 60 μm, consistent with the trends observed in the whole-brain microvascular quantitative analysis.

3.7. Behavioral performance of septic mice in motor and cognitive memory tests

To correlate the findings from microvascular pathological analysis in major brain regions, we assessed motor function and cognitive memory in septic mice 5 days after CLP surgery using the OFT[15]and NOR[39].

Based on the OFT results, septic mice exhibited significant behavioral alterations 5 days post-CLP surgery. Compared to the Sham group, the CLP group showed significantly reduced movement speed and total travel distance, indicating substantial impairment in motor function. Furthermore, the CLP group spent significantly less time in the central zone, suggesting affected exploratory behavior and anxiety levels. These results demonstrate markedly diminished motor capacity and exploratory activity in septic mice, which may correlates with the observed damage in M1/M2 brain regions.

According to NOR findings, septic mice displayed significant cognitive dysfunction 5 days post-CLP. The CLP group showed significantly lower discrimination index and recognition index values compared to Sham controls, indicating substantial cognitive impairment. Recognition index reflects the proportion of the time spent exploring the new object relative to the total exploration time, thereby capturing the overall preference of mice for new things. In contrast, discrimination index reflects the time difference between mice on new object and familiar object, measuring the animals' ability to distinguish. When considered alongside the pathological changes in the RSD region, these results suggest that while cognitive function was significantly compromised in septic mice, the degree of impairment was less severe than motor deficits. This observation corresponds with the microvascular pathological analysis of relevant brain regions.

4. Discussion

Mounting evidence indicates that brain injury plays a pivotal role in the pathogenesis of sepsis and is strongly correlated with mortality rates. However, the relationship between microvascular pathological changes and sepsis progression remains unclear. In this investigation, we employed photoacoustic imaging technology to conduct in *vivo* imaging and perform comprehensive quantitative analyses. Through the classic EB experiment, we observed BBB damage in septic mice and revealed vascular network characteristics at 24 hours and 7 days post-CLP.

The CLP model effectively induces sepsis-associated neuroinflammation and BBB disruption. The results from speckle imaging revealed most significant cerebral blood flow alterations at 6 hours post-CLP. Pro-inflammatory cytokines IL-6 and TNF-α were significantly elevated in the CLP group, as well as liver and kidney damage markers were also significantly increased, suggesting an early stages of SAE.

Literature indicates that pro-inflammatory factors like TNF-α and IL-17A, as well as the microglial activation marker ionized calcium-binding adapter molecule 1, are significantly elevated at this time, suggesting early inflammation and microglial activation[40]. Zona occludens 1 and occludin, key proteins maintaining BBB integrity, are significantly reduced at 6 hours post-CLP[41]. These findings confirm that SAE pathological changes are detectable at 6 hours post-CLP, allowing investigation of BBB disruption while avoiding late-stage mortality effects.

The PAI results showed that at 6 hours post-CLP surgery, septic mice exhibited severe BBB damage with significantly increased permeability, manifested by enhanced EB diffusion extent and accelerated diffusion rate. Notably, compared to sham-operated controls which showed minimal EB leakage, septic mice exhibited extensive EB extravasation in the cortical region. This point was further confirmed through postmortem brain dissection, which demonstrated clear evidence of EB leakage from cortical vasculature into the brain parenchyma of septic mice.

At 24 hours post-CLP, the vascular network characteristics showed no significant differences between septic and sham-operated mice. However, at 7 days post-CLP, some cerebrovascular pathological changes can be observed in septic mice, including decreased vascular density and branching index (indicating reduced vascular complexity), increased porosity and tortuosity, reduced vascular network homogeneity with extensive vacant areas, as well as an increased proportion of thin vessels and decreased proportion of thick vessels, suggesting a vasoconstriction trend.

A more detailed analysis of vascular pathological changes in major cortical regions revealed consistent BBB damage across all examined brain areas in septic mice, with particularly severe damage observed in the M1/M2 cortical regions. While vascular network alterations followed similar patterns to whole-brain changes in all regions, the M1/M2 areas exhibited the most pronounced modifications, correlating precisely with the most severe BBB impairment. Subsequent behavioral evaluations using both the OFT and NOR test demonstrated significant deterioration in both motor and cognitive functions in septic mice. These functional deficits showed strong correspondence with the pathological changes observed in the M1/M2 and RSD cortical regions.

A limited number of studies have employed in vivo imaging techniques such as magnetic resonance imaging to quantitatively analyze parenchymal changes in different brain regions of septic mice, or utilized second near-infrared imaging with contrast agents to investigate microvascular alterations. However, constrained by the resolution limitations of current imaging modalities, no studies to date have conducted comprehensive quantitative analysis of the pathological changes in microvasculature during sepsis.

This study utilized in vivo PAI with blood as an endogenous contrast agent to obtain high-resolution microvascular network images at micron-scale. We performed comprehensive quantitative analyses linking BBB impairment and vascular morphological changes in major cortical regions of septic mice, with behavioral tests validating these analytical results. Our findings provide novel research perspectives and experimental evidence for understanding the relationship between microvascular pathology and disease progression in sepsis.

However, the current study only evaluated morphological characteristics of cortical microvascular networks. Future research will assess additional pathological and physiological functional parameters, such as blood oxygen saturation, and their correlations with disease progression. PAM's high specificity and contrast enable imaging of multiple biomarkers in biological tissues. For instance, in brain disease research, PAM can provide novel insights when combined with in vivo imaging of meningeal lymphatic vessels[17]. Furthermore, PAM enhanced with deep learning techniques can achieve cellular-level imaging without exogenous labels, potentially replacing immunofluorescence methods [42]. In recent years, PAI has advanced rapidly, demonstrating significant potential for clinical and commercial translation[43]. Additionally, with the advantage of imaging depth of photoacoustic computed tomography, non-invasive in vivo imaging of deep brain structures could be achieved[44].When combined with ultrasound imaging, photoacoustic computed tomography can also deliver hemodynamic parameters[45] such as cerebral blood volume and cerebral blood flow [46–48].

5. Conclusion

In summary, our study leveraged the high-resolution microvascular network images provided by PAI to conduct a comprehensive, multi-dimensional quantitative analysis of cerebrovascular pathology in septic mice, with behavioral experiments corroborating these analytical findings. Although further studies are needed to determine region-specific cerebrovascular pathological changes during sepsis progression, the non-invasive PAI-based regional fractal analysis of cerebral microvasculature has emerged as a promising approach for assessing sepsis progression and therapeutic efficacy, providing a valuable tool for future research and clinical applications.

CRediT authorship contribution statement

Ting Sun: Writing – review & editing, Writing – original draft, Investigation. **Zhiyang Wang:** Writing – review & editing, Formal analysis. **Wuyu Zhang:** Writing – review & editing, Software. **Feifan Zhou:** Supervision, Methodology, Funding acquisition, Conceptualization. **Zhigang Wang:** Writing – review & editing, Writing – original draft, Investigation, Formal analysis. **Changpeng Ai:** Writing – review & editing, Writing – original draft, Investigation, Formal analysis. **Shengnan Wu:** Supervision, Methodology, Conceptualization.

Declaration of Competing Interest

The authors declare that they have no known competing financial interests or personal relationships that could have appeared to influence the work reported in this paper.

Acknowledgements

This work was supported by STI2030- Major Projects (2022ZD0212200), Hainan Province Key Area R&D Program (KJRC2023C30).

Data availability

Data will be made available on request.

References

[1] M. Singer, C.S. Deutschman, C.W. Seymour, et al., The third international consensus definitions for sepsis and septic shock (Sepsis-3) [J], Jama 315 (8) (2016) 801–810.
[2] K.E. Rudd, S.C. Johnson, K.M. Agesa, et al., Global, regional, and national sepsis incidence and mortality, 1990-2017: analysis for the global burden of disease study [J], Lancet (Lond., Engl.) 395 (10219) (2020) 200–211.
[3] C.N. Widmann, M.T. Heneka, Long-term cerebral consequences of sepsis [J], Lancet Neurol. 13 (6) (2014) 630–636.
[4] R. Sonneville, E. de Montmollin, J. Poujade, et al., Potentially modifiable factors contributing to sepsis-associated encephalopathy [J], Intensive care Med. 43 (8) (2017) 1075–1084.
[5] T.E. Gofton, G.B. Young, Sepsis-associated encephalopathy [J], Nat. Rev. Neurol. 8 (10) (2012) 557–566.
[6] S. Pan, Z. Lv, R. Wang, et al., Sepsis-Induced Brain Dysfunction: Pathogenesis, Diagnosis, and Treatment [J], Oxid. Med. Cell. Longev. 2022 (2022) 1328729.
[7] F.A. Bozza, P. Garteiser, M.F. Oliveira, et al., Sepsis-associated encephalopathy: a magnetic resonance imaging and spectroscopy study [J], J. Cereb. Blood Flow. Metab.: Off. J. Int. Soc. Cereb. Blood Flow. Metab. 30 (2) (2010) 440–448.
[8] Y. Imamura, S. Yamada, S. Tsuboi, et al., Near-infrared emitting PbS quantum dots for in vivo fluorescence imaging of the thrombotic state in septic mouse brain [J], Mol. (Basel, Switz.) 21 (8) (2016).

[9] Z. Wang, F. Yang, W. Zhang, et al., Towards in vivo photoacoustic human imaging: shining a new light on clinical diagnostics [J], Fundam. Res. 4 (5) (2024) 1314–1330.
[10] W. Zhang, X. Luo, F. Yang, et al., Photoacoustic (532 and 1064 nm) and ultrasonic coscanning microscopy for in vivo imaging on small animals: a productized strategy [J], J. biophotonics 16 (6) (2023) e202300007.
[11] H. Qu, J. Wu, Y. Pan, et al., Biomimetic nanomodulator regulates oxidative and inflammatory stresses to treat sepsis-associated encephalopathy [J], ACS nano 18 (41) (2024) 28228–28245.
[12] L. Zhao, Z. Zhang, P. Wang, et al., NHH promotes sepsis-associated encephalopathy with the expression of AQP4 in astrocytes through the gut-brain axis [J], J. Neuroinflamm. 21 (1) (2024) 138.
[13] E. Zudaire, L. Gambardella, C. Kurcz, et al., A computational tool for quantitative analysis of vascular networks [J], PloS One 6 (11) (2011) e27385.
[14] T. Guo, K. Xiong, B. Yuan, et al., Homogeneous-resolution photoacoustic microscopy for ultrawide field-of-view neurovascular imaging in Alzheimer's disease [J], Photoacoustics 31 (2023) 100516.
[15] Kraeuter A.K., Guest P.C., Sarnyai Z. The Open Field Test for Measuring Locomotor Activity and Anxiety-Like Behavior [J]. Methods in molecular biology (Clifton, NJ), 2019, 1916: 99-103.
[16] X. Li, Z. Zhang, H. Shi, et al., Characterization of cerebrovascular changes in Alzheimer's disease mice by photoacoustic imaging [J], J. Innov. Opt. Health Sci. 17 (06) (2024) 2450007.
[17] F. Yang, Z. Wang, W. Shi, et al., Advancing insights into in vivo meningeal lymphatic vessels with stereoscopic wide-field photoacoustic microscopy, J.]. Light, Sci. Appl. 13 (1) (2024) 96.
[18] F. Yang, Z. Wang, W. Zhang, et al., Wide-field monitoring and real-time local recording of microvascular networks on small animals with a dual-raster-scanned photoacoustic microscope [J], J. biophotonics 13 (6) (2020) e202000022.
[19] T. Csipo, B.R. Cassidy, P. Balasubramanian, et al., Endothelial Dysfunction and Impaired Neurovascular Coupling Responses Precede Cognitive Impairment in a Mouse Model of Geriatric Sepsis [J], Front. Aging Neurosci. 13 (2021) 644733.
[20] K. Erikson, H. Tuominen, M. Vakkala, et al., Brain tight junction protein expression in sepsis in an autopsy series [J], Crit. care (Lond., Engl.) 24 (1) (2020) 385.
[21] K. Wang, M. Sun, Z. Juan, et al., The Improvement of sepsis-associated encephalopathy by P2X7R inhibitor through inhibiting the Omi/HtrA2 apoptotic signaling pathway [J], Behav. Neurol. 2022 (2022) 3777351.
[22] L. Liu, H. Zhang, Y. Shi, et al., Prostaglandin E1 improves cerebral microcirculation through activation of endothelial NOS and GRPCH1 [J], J. Mol. neuro Sci.: MN 70 (12) (2020) 2041–2048.
[23] M. Gu, X.L. Mei, Y.N. Zhao, Sepsis and cerebral dysfunction: BBB damage, neuroinflammation, oxidative stress, apoptosis and autophagy as key mediators and the potential therapeutic approaches [J], Neurotox. Res. 39 (2) (2021) 489–503.
[24] R. Cao, J. Li, C. Zhang, et al., Photoacoustic microscopy of obesity-induced cerebrovascular alterations [J], NeuroImage 188 (2019) 369–379.
[25] B. Engelhardt, L. Sorokin, The blood-brain and the blood-cerebrospinal fluid barriers: function and dysfunction [J], Semin. Immunopathol. 31 (4) (2009) 497–511.
[26] L.A. Opperman, Cranial sutures as intramembranous bone growth sites [J], Dev. Dyn.: Off. Publ. Am. Assoc. Anat. 219 (4) (2000) 472–485.
[27] B. Schaller, Physiology of cerebral venous blood flow: from experimental data in animals to normal function in humans [J], Brain Res. Brain Res. Rev. 46 (3) (2004) 243–260.
[28] C.S. Burkhart, M. Siegemund, L.A. Steiner, Cerebral perfusion in sepsis [J], Crit. care (Lond., Engl.) 14 (2) (2010) 215.
[29] M.D. Sweeney, K. Kisler, A. Montagne, et al., The role of brain vasculature in neurodegenerative disorders [J], Nat. Neurosci. 21 (10) (2018) 1318–1331.
[30] A. Montagne, Z. Zhao, B.V. Zlokovic, Alzheimer's disease: A matter of blood-brain barrier dysfunction? [J], J. Exp. Med. 214 (11) (2017) 3151–3169.
[31] C. Iadecola, The neurovascular unit coming of age: a journey through neurovascular coupling in health and disease [J], Neuron 96 (1) (2017) 17–42.
[32] T. Barichello, J.J. Fortunato, A.M. Vitali, et al., Oxidative variables in the rat brain after sepsis induced by cecal ligation and perforation [J], Crit. care Med. 34 (3) (2006) 886–889.
[33] R.N. Lemon, Descending pathways in motor control [J], Annu. Rev. Neurosci. 31 (2008) 195–218.
[34] O. Hikosaka, K. Nakamura, H. Nakahara, Basal ganglia orient eyes to reward [J], J. Neurophysiol. 95 (2) (2006) 567–584.
[35] B.W. Balleine, M.R. Delgado, O. Hikosaka, The role of the dorsal striatum in reward and decision-making [J], J. Neurosci.: Off. J. Soc. Neurosci. 27 (31) (2007) 8161–8165.
[36] D.H. Hubel, T.N. Wiesel, Receptive fields, binocular interaction and functional architecture in the cat's visual cortex [J], J. Physiol. 160 (1) (1962) 106–154.
[37] W. Roe A, Y. Ts'o D, Visual topography in primate V2: multiple representation across functional stripes [J], J. Neurosci.: Off. J. Soc. Neurosci. 15 (5 Pt 2) (1995) 3689–3715.
[38] E.S. Lein, M.J. Hawrylycz, N. Ao, et al., Genome-wide atlas of gene expression in the adult mouse brain [J], Nature 445 (7124) (2007) 168–176.
[39] M. Leger, A. Quiedeville, V. Bouet, et al., Object recognition test in mice [J], Nat. Protoc. 8 (12) (2013) 2531–2537.
[40] B. Ye, T. Tao, A. Zhao, et al., Blockade of IL-17A/IL-17R pathway protected mice from sepsis-associated encephalopathy by inhibition of microglia activation [J], Mediat. Inflamm. 2019 (2019) 8461725.
[41] Y. Jiang, K. Zhang, Y. Yu, et al., Molecular hydrogen alleviates brain injury and cognitive impairment in a chronic sequelae model of murine polymicrobial sepsis [J], Exp. brain Res. 238 (12) (2020) 2897–2908.
[42] E. Park, S. Misra, D.G. Hwang, et al., Unsupervised inter-domain transformation for virtually stained high-resolution mid-infrared photoacoustic microscopy using explainable deep learning [J], Nat. Commun. 15 (1) (2024) 10892.
[43] J. Park, S. Choi, F. Knieling, et al., Clinical translation of photoacoustic imaging [J], Nat. Rev. Bioeng. 3 (3) (2025) 193–212.
[44] H. Xu, Z. Chen, Y. Wu, et al., Noninvasive high-resolution deep-brain photoacoustic imaging with a negatively focused fiber-laser ultrasound transducer [J], Photonics Res. 12 (12) (2024).
[45] H. Chen, S. Mirg, P. Gaddale, et al., Multiparametric brain hemodynamics imaging using a combined ultrafast ultrasound and photoacoustic system [J], Adv. Sci. 11 (31) (2024).
[46] J. Kim, J.Y. Kweon, S. Choi, et al., Non-invasive photoacoustic cerebrovascular monitoring of early-stage ischemic strokes in vivo [J], Adv. Sci. (Weinh., Baden. -Wurtt., Ger.) 12 (4) (2025) e2409361.
[47] L. Menozzi, T. Vu, A.J. Canning, et al., Three-dimensional diffractive acoustic tomography [J], Nat. Commun. 16 (1) (2025) 1149.
[48] L. Menozzi, Á. Del Águila, T. Vu, et al., Three-dimensional non-invasive brain imaging of ischemic stroke by integrated photoacoustic, ultrasound and angiographic tomography (PAUSAT) [J], Photoacoustics 29 (2023) 100444.

Zhigang Wang is a master's student in the College of Biophotonics, School of Optoelectronic Science and Engineering at South China Normal University. His research interests are focused on multimodal photoacoustic microscopy imaging system and its application in neuroscience

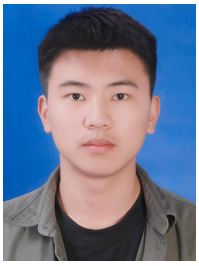

Changpeng Ai is a master's student at the School of Medical Technology, Beijing Institute of Technology. His research interests are focused on the biological effects of light.

Ting Sun is a PhD student at the School of Biomedical Engineering at Hainan University. Her research focuses on the use of photoacoustic imaging in the cerebrovascular and lymphatic systems of the brain.

Zhiyang Wang is a postdoctoral fellow in the College of Biophotonics, School of Optoelectronic Science and Engineering at South China Normal University. His research interests are focused on photoacoustic microscopy and its clinical applications.

Feifan Zhou is a professor at the School of Biomedical Engineering, Hainan University. Her research focuses on neuroimmune visualization and regulation.

Wuyu Zhang is a postdoctoral fellow in the College of Biophotonics, School of Optoelectronic Science and Engineering at South China Normal University. His research interests are focused on instrumentation application and translation of photoacoustic microscopy imaging technology

Shengnan Wu is a professor at the School of Medical Technology, Beijing Institute of Technology. Her research primarily focuses on the mechanisms of photobiological effects in novel non-invasive phototherapy.